

# Sinkhole characterization in the Dead Sea area using airborne laser scanning

Sagi Filin · Amit Baruch · Yoav Avni · Shmuel Marco

Received: 23 April 2010 / Accepted: 6 January 2011 / Published online: 28 January 2011  
© Springer Science+Business Media B.V. 2011

**Abstract** Since the early 1980s, the Dead Sea coast has undergone a near catastrophic land deterioration as a result of a rapid lake-level drop. One conspicuous expression of this deterioration is the formation of sinkholes fields that puncture the coastal plains. The evolution of sinkholes along nearly 70-km strip has brought to a halt the regional development in this well-known and toured area and destroyed existing infrastructures. Great efforts are being invested in understanding the phenomena and in development of monitoring techniques. We report in this paper the application of airborne laser scanning for characterization of sinkholes. We demonstrate first the appropriateness of laser scanning for this task and its ability to provide detailed 3D information on this phenomenon. We describe then an autonomous means for their extraction over large regions and with high level of accuracy. Extraction is followed by their detailed geometric characterization. Using this high-resolution data, we show how sinkholes of 0.5 m radius and 25 cm depth can be detected from airborne platforms as well as the geomorphic features surrounding them. These sinkhole measures account for their embryonic stage, allowing tracking them at an early phase of their creation.

**Keywords** Sinkholes · Airborne laser scanning · Dead Sea · Land degradation

---

S. Filin (✉) · A. Baruch  
Department of Civil and Environmental Engineering, Technion - Israel Institute of Technology,  
Haifa, Israel  
e-mail: filin@technion.ac.il

A. Baruch  
e-mail: amit@technion.ac.il

Y. Avni  
Geological Survey of Israel, 95501 Jerusalem, Israel  
e-mail: yavni@gsi.gov.il

S. Marco  
Department of Geophysics and Planetary Sciences, Tel-Aviv University,  
69978 Tel-Aviv, Israel  
e-mail: shmulikm@tau.ac.il

## 1 Introduction

The Dead Sea region (Fig. 1), the lowest place on the Earth continents, is an active morphotectonic depression. The depression is a pull-apart basin that was formed where two segments of the left-lateral Dead Sea Transform fault (DST in Fig. 1) overlap. The Dead Sea itself is a terminal hypersaline lake that occupies the lowest part of the depression and drains an area of 40700 km<sup>2</sup>. During the middle 20th century, the lake was at a level of 392 m below mean sea level (m.b.m.s.l), but since the mid-1960s, increased diversion of water from its northern drainage basin accelerated the drop in the lake level, reaching an average rate of 1 my<sup>-1</sup>. The 2010 level is 423 m.b.m.s.l.

The rapid drop in the lake level undermines the stability of the geomorphic systems around the Dead Sea and triggers a chain of reactions with a disastrous impact and environmental deterioration along the coastal plains, featured in soil erosion, incision of channels, rapid headcut migration, and development of collapse sinkhole fields. At the beginning of the 1980s, collapse sinkholes began appearing along the Dead Sea coastal plains, both in the Israeli and the Jordanian sides. The formation rate has accelerated since

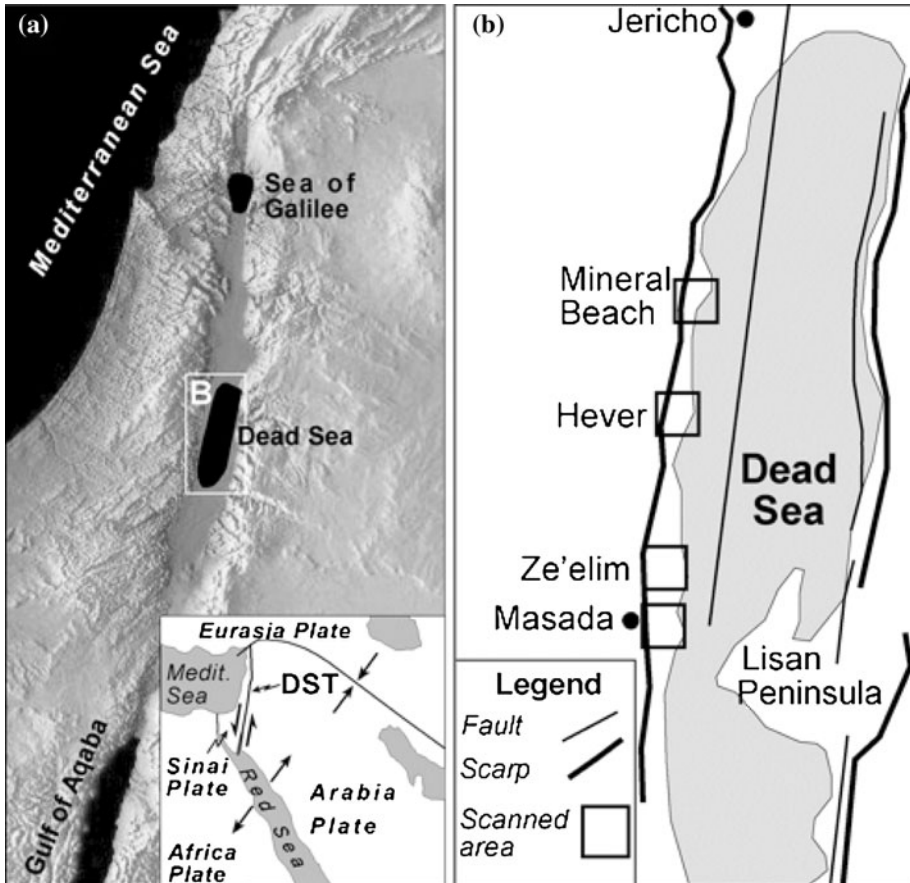


**Fig. 1** Location map of the surveyed sites: **a** shaded relief map (Hall 1994) showing main strands of the Dead Sea Transform (DST) in the region. *Inset* shows the tectonic plate setting, **b** location of scanned areas

the early 2000s; hundreds of them can be found nowadays along large parts of the coast (Abelson et al. 2006). In most cases, sinkholes appear first in an embryonic form of about 1 m, and later, they can evolve into large fields that may reach up to 100 sinkholes within a single site. Several linear groups of sinkholes are interpreted as being controlled by active faults (Abelson et al. 2006). As a consequence of their appearance, regional development has come to a halt in some areas, and as they endanger the stability of the present infrastructure they pose severe threat to the future development of the region. Similar reports on sinkhole effect in other parts of the world can be found in Nichol (1998), Kaufmann and Quinif (2002), and in Buttrick and Schalkwyk (1998), where the loss of property and human lives due to sinkhole formation are reported. However, in most of these reported cases, the collapse sinkholes developed as a result of carbonate or gypsum dissolution, a much slower process relative to the dissolution of halite in the Dead Sea basin.

The study of active rapid processes, such as sinkhole formation, necessitates means for tracing, quantifying, and finally, monitoring of their evolution. Such means should facilitate the coverage of wide regions and provide detailed information on the undergoing changes. Sinkholes and their environments along the Dead Sea coastal plains have been analyzed by various sensing techniques (Baer et al. 2002; Closson et al. 2003; Abelson et al. 2003; Closson 2005) with sinkholes being explored using aerial photography and land surveying (e.g., Yechieli et al. 2003; Abelson et al. 2006). Using these methods, it is hard to detect small embryonic sinkholes, or distinguish between actual depressions and artificial, image-related intensity effects with a sinkhole-like appearance (e.g., shadowing, shrubs; similar conclusion is also reached by Kaufmann and Quinif 2002).

We report the use of laser scanning technology as a complimentary means for the detection and characterization of sinkholes. We test the level of detection that laser scanning systems offer and the added information that can be retrieved from the data. Further to validating the ability to capture topographic anomalies as sinkholes offer, we test autonomous sinkhole detection over large regions. Although sinkholes are widespread, they occupy only a small fraction of the overall area. They appear both in isolated occurrences and in clusters, and in various shapes and forms, ranging from small and shallow (mostly at their formation stage), and into well-developed broad and deep entities. Furthermore, they have been forming in different environments, e.g., vegetated or cluttered, and in different sedimentary environments that can be either smooth fine-grained, or roughly textured, particularly within the alluvial fans. The paper also demonstrates the advantage of laser scanning for detection and analysis over image-based techniques, demonstrating among other things sinkholes extraction under tree canopies.

We begin the presentation with a short overview of the sinkhole phenomena and demonstrate their expression along the coastal plains. We then propose a methodology for sinkhole detection and characterization. The presentation shows the ability to detect sinkholes in various forms in high level of success, while overcoming the complex environment that surround them. Following the presentation of the proposed model, results and analysis that demonstrate extraction and characterization abilities come, ending with conclusions.

## 2 Sinkholes formation and expression

The emergence of collapse sinkholes along the Dead Sea coastal plains can be ascribed to the rapid lake-level drop, which is mainly linked to the intervention in the Jordan River

flow (controlling fresh water flow) and to the Dead Sea mineral industries that use the Dead Sea water for their needs (Abelson et al. 2006). As a result of a subsurface process in which a thick layer of salt, located at present in a depth of 20–50 m below surface, dissolved by fresh water running toward the receding lake, subsurface caverns were formed (Yechieli et al. 2003; Abelson et al. 2006; Yechieli et al. 2006). The expansion of the caverns through time leads to the collapse of the surface above it, thereby forming an embryonic sinkhole that can, over time, develop into a field comprising of swarms of sinkholes. Sinkholes can be observed in two main sedimentary environments along the coast of the Dead Sea, the mudflats, and the alluvial fans. A single sinkhole can reach a diameter of 25 m and extend to a depth of 20 m. Along the Dead Sea coast, sinkholes have been observed along a ~70-km-long strip, with embryonic sinkholes of <1 m diameter. It is noted that in the Lisan Formation outcrops, west of the coast, sinkholes have been forming due to other processes, where subsurface flow through unconsolidated alluvial material, especially fine-grained clay, led to the creation of subsurface horizontal pipes that collapsed to form up-surface sinkholes (Arkin and Gilat 2000). Reports on similar mechanisms in other parts of the world, attributing sinkhole formation to subterranean cavities formed by dissolution within layers of soluble rocks can also be found in Martínez et al. (1998), Tharp (1999), Neal and Johnson (2002), and Salvati and Sasowsky (2002).

The environmental impact of sinkholes on the Dead Sea region is demonstrated in Fig. 2. Figure 2a features a well-developed sinkhole field near a beach resort, including a cluster of sinkholes all of considerable size, which at this stage begun collapsing into one another. Figure 2b shows an isolated sinkhole that evolved within a palm plantation; such sinkhole and others have brought to a halt the agricultural cultivation there. Figure 2c, d shows sinkhole fields taken from low altitude aerial images; in Fig. 2c, a field featuring sinkholes of diverse characteristics in terms of size, shape, and depth can be seen, and in Fig. 2d, sinkholes were formed within a parking lot of a beach resort. One can notice the extent of destruction that has led to the abandonment of this popular beach resort.

### 3 Detection

Collapse sinkholes can be described as surface depressions relative to the surrounding terrain. Therefore, their detection can be approached by first seeking inner sinkhole (depression related) points within the data and localize on their outline. Their concave shape can be modeled by the second-order partial derivatives, as arranged by the Hessian form,  $\mathbf{H}$

$$\mathbf{H} = \begin{bmatrix} Z_{xx} & Z_{xy} \\ Z_{xy} & Z_{yy} \end{bmatrix} \quad (1)$$

with  $Z$  the heights as derived from the laser scanning data. For a stationary point to be locally minimal and concave in all directions,  $\mathbf{H}$  must be positive-definite, namely, having both eigenvalues positive.  $\mathbf{H}$  is assembled by convolving a set of directional second-order derivative filters on the data, computing  $Z_{xx}$ ,  $Z_{yy}$ , and  $Z_{xy}$ . A numerical computation of the derivatives—namely,  $Z_{xx} = (Z_{y_0, x_0+d} - 2Z_{y_0, x_0} + Z_{y_0, x_0-d})/d^2$  etc., with  $d$  the filter size—has proved optimal for the analysis (this is in contrast to analytical, local surface-fitting-based approach, e.g., Besl 1988).

Because of the variety of forms (size and depth) and surface texture characteristics (ranging from relatively smooth to rough), the detection must consider phenomena of



**Fig. 2** Sinkholes: **a** a field near the Mineral Beach resort, **b** a solitary sinkhole that formed within a palm plantation, **c** an aerial view of a sinkhole field; the encircled area refers to the sinkholes shown in ‘a’, **d** a sinkholes in a parking lot of a beach resort near the Ein-Gedi oasis; following their formation, this resort was abandoned

different magnitude and be robust to the surface roughness. To accommodate form variation, the detection is performed in multiple scales, by applying a family of filters with different support, and searching for responses that are strong enough to mark points as sinkhole candidates. For small windows, which focus on modest-size sinkholes, robustness to background surface texture and noise is supported by setting lower detection response level on the obtained eigenvalues. The general requirement is for  $\lambda > 0$ , or more precisely  $\lambda_{\max} \geq \lambda_{\min} > \epsilon$ . Using accuracy estimates for the elevation and propagating it, detection limits can be set for the minimal eigenvalue

$$\lambda_{\min} > z(1 - \alpha)m_\lambda \Rightarrow \lambda_{\min} > z(1 - \alpha)\frac{\sqrt{6}}{d^2}m_z = 1.65\frac{\sqrt{6}}{d^2}m_z \quad (\alpha = 5\%) \quad (2)$$

with  $z$ , the normalized Gaussian distribution, and  $m_z$ , the elevation accuracy as derived from the laser data.

The detected seed points act as topographic markers for the inner sinkhole part. Their boundary localization is handled by requiring a closed polygonal form, preferably smooth, which follows the transition from the inner sinkhole part to the surrounding terrain. This transition is identified, in most cases, by a change in the gradient value. Both shape and boundary constraints are accommodated when cast as an energy minimization problem in which the sinkhole border is modeled as an active contour (Kass et al. 1988) whose shape is guided by internal spline, and external boundary forces. Representing the contour location as  $x(s)$ , with  $s$  as the arc-length parameter, its energy functional can be written as

$$E_c = \int_0^1 E_c(x(s))ds = \int_0^1 E_{\text{int}}(x(s)) + E_{\text{ext}}(x(s))ds \quad (3)$$

with  $E_c$ , the contour energy,  $E_{\text{int}}$ , the internal spline energy due to bending, and  $E_{\text{ext}}$ , the external energy arriving from the terrain (by means of the laser scanning data). Since the internal energy is influenced by the spline setup, the external energy is what drives the contour to its actual boundary.

The extracted sinkhole candidates reflect intrinsic properties that stem from detection of a local surface depression and evolution of the bounding curve into its natural boundary. Candidates then undergo validation tests that analyze their boundary and depth parameters in order to evaluate their distinctiveness compared to the surrounding. The applied set of tests is detailed in the Appendix.

#### 4 Analysis and discussion

Laser-scanning based detection and characterization is studied in four different localities along the coastal plains (Fig. 1), each offering unique/individual surface characteristics and features. The surveyed regions include (i) the *Ze'elim and Hever fans* (lat. 31°22', long. 35°24' and lat. 31°20', long. 35°25' of both sites, respectively)—two of the largest fans developed during the late Pleistocene-Holocene along the Dead Sea western coast, where sinkholes have been developing both in alluvial and mudflats surface; (ii) the *Ein-Gedi oasis* (lat. 31°27', long. 35°23')—where the appearance of sinkholes had severe impact on agricultural activities and regional development; and (iii) *Mineral Beach* (lat. 31°32', long. 35°23')—where anthropogenic infrastructure was severely damaged and further endangered by sinkholes and gullies.

Laser scanning data were acquired using the Optech 2050 scanner, operating at flying altitude of ~500 m above ground level and at pulse transmission rate of 50 kHz. The resulting point density was ~4 points/m<sup>2</sup> and in overlapping regions between swaths reached ~6 point/m<sup>2</sup>. Data accuracy was evaluated by 250 ground reference points that were measured using the new Israeli GPS virtual real-time network, as a reference station. Height accuracy was ±10 cm. Validation of the geomorphic features was carried out by field surveys in all three locations. Validation included qualitative, inventory study and additional relative measures, where possible. No anomalous behavior or any artifacts have

been identified, and all studied features that appeared in the laser scanning data have been observed in the studied sites.

#### 4.1 Expression of sinkholes in the data

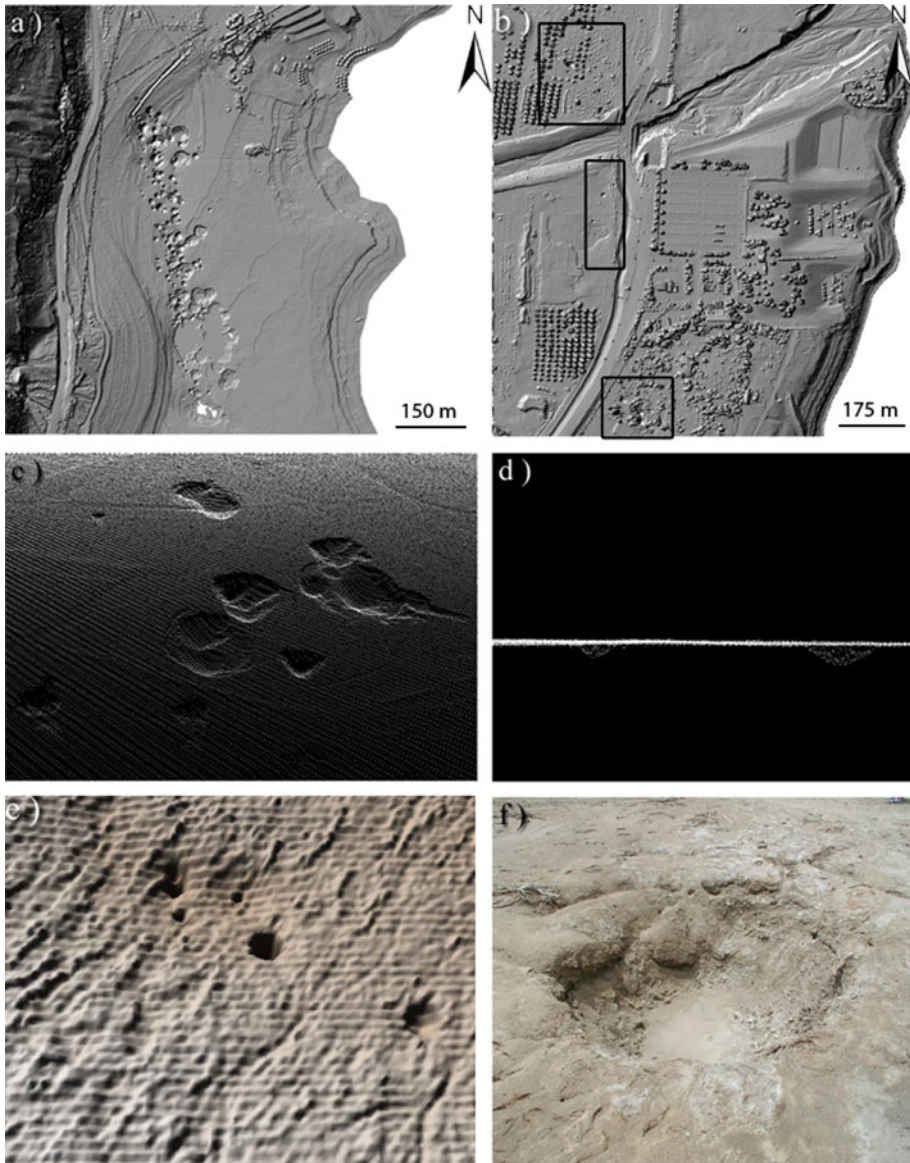
Sinkholes expression in the laser survey is demonstrated via shaded relief maps and 3D views of the point cloud and the reconstructed surface (Fig. 3). The data shown in Fig. 3a correspond to sinkholes in Fig. 2c and show their clear expression. Some signs of the lake retreat can be noticed there, particularly the linear beach terraces. Near the Ein-Gedi oasis (Fig. 3b), three sinkhole clusters are shown delimited, one is within a palm plantation (cf. Fig. 2b), and others are within a parking lot of a beach resort. Sinkholes actual expression within the point cloud is featured in Fig. 3c, d, showing how subtle their appearance may be. An embryonic  $\sim 1$  m diameter,  $\sim 50$  cm deep, sinkhole that was formed in the mudflats (exposed lakebed following the lake retreat) is shown in Fig. 3e, f. Demonstrated is not only their expression within the laser scanning data, but also existence of modest-size solitary features. One can also notice the minute details that the laser scanning captures, e.g., concentric cracks developed around the sinkholes, which are caused by collapse of the surface onto the expanding cavity, and collapse of the surrounding walls (Fig. 4), both features indicate their ongoing evolution.

Another major advantage of utilizing laser scanning technology is the canopy penetration ability. A notable example is demonstrated in Fig. 5 where an aerial image shows no evidence of sinkholes, and the shaded relief map of the laser scanning data indicates the existence of only one (Fig. 5a, b). However, following data filtering (Akell et al. 2007) that is aimed at separating off-terrain returns (tree canopies here), three additional sinkholes within palm plantation are revealed (Fig. 5c). A side-looking view of the point cloud (Fig. 5d) shows their existence.

#### 4.2 Extraction of sinkhole properties

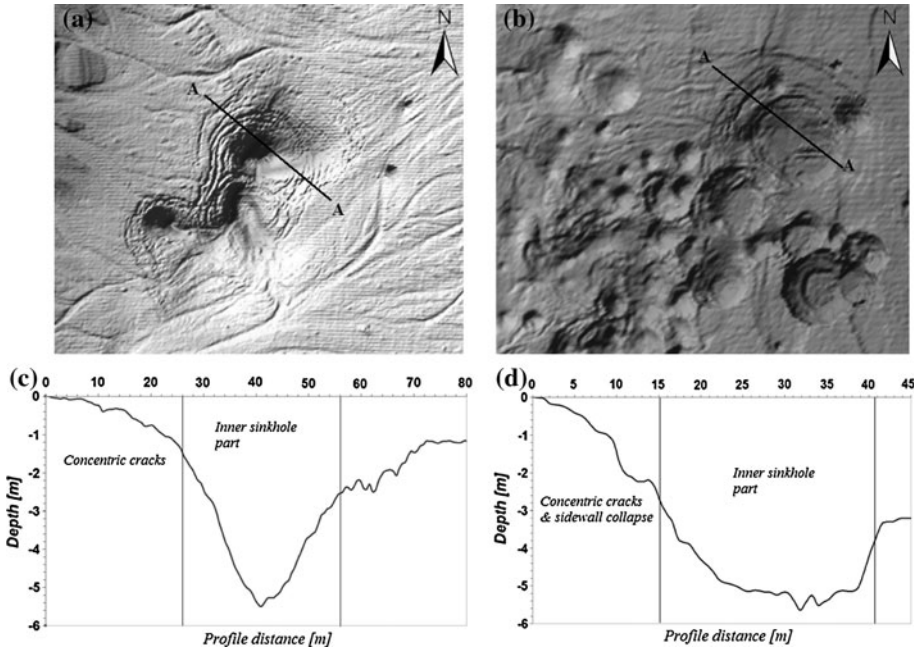
The application of the model is demonstrated in detail on sinkholes with characteristic geometries and depth. Sinkholes in two regions are selected, including the *i*) Mineral Beach mudflats where sinkholes size (diameter and depth) is small and transition is not always clear and *ii*) an abandoned parking lot near the Ein-Gedi beach resort featuring clutter that mixes sinkholes, small pits, trees, and low vegetation. Fig. 6a shows a sector within the Mineral beach region with two bowl-like shape sinkholes (Fig. 6b). The detected seed points capture the inner part of the sinkhole, and the closed curves surrounding them illustrate contour evolution until convergence to the boundary is reached. In Fig. 6c, sinkholes that have been forming in a fine-grained sedimentary environment (Abelson et al. 2006) can be seen. The collapse there is abrupt (see Fig. 6d), and the sinkholes depth ranges between 2 and 6 m. The abrupt drop in the surface is clearly manifested in the rightmost sinkhole where the seed points from which the sinkhole spline evolves are already near the outermost contour. The subsequent refinements that the contour undergoes relate both to the convergence to the sinkhole boundary and to the shape refinement, which minimizes the curve energy.

Figure 7 shows sinkholes demarcation resulting from the detection process on the mineral beach scan. Notice a cluster of sinkholes, where some began collapsing into one another. Because of the inner seed point detection, the model has managed identifying the individual sinkholes and to converge into what appears as the natural surrounding edge. The concentric cracks that surround the sinkhole clusters there offer an insight into future



**Fig. 3** Sinkholes expression in airborne laser scanning data: **a** a shaded relief map of a sinkhole field along Mineral Beach (shown also in Fig. 2c), **b** sinkholes in the Ein-Gedi oasis, within a palm plantation (*top*) and within a now-abandoned parking lot (*bottom*), **c** sinkholes expression within the 3D point cloud, **d** a side-looking view of two 60-cm-deep solitary sinkholes, **e** a perspective view derived from the laser point cloud of embryonic sinkholes, **f** an actual view of a small sinkhole 0.3 m deep

evolution of this field. Southwards, but still in that region, Fig. 7b shows a typical example of sinkhole development in a relatively smooth region. Sinkholes in this area are relatively small and shallow, with size ranging between 0.41 and 1.76 m in depth and between 2 and 6 m in diameter. The detection results (Fig. 7b) show that despite their shallow depth and



**Fig. 4** Expressions of concentric cracks and sidewall collapse in the laser scanning data: **a** a shaded relief map of a sinkhole with tension rings in the Ze’elim fan; **b** a shaded relief map showing concentric cracks and sidewall collapse; **c** and **d** extracted profiles showing height variations of these phenomena

the relatively smooth transition, the contour-seeking model managed following the sinkholes boundary. Contrasting the Mineral Beach mudflats, the second area in which the demarcation is demonstrated (within the Hever fan, Fig. 8), offers rough textured surfaces dissected by streams. Sinkholes have evolved there within a gravelly alluvial fan with a broad span of braided streams, contributing to a rough surface texture that increases the already strong background noise. The deepest sinkhole in this region reaches 18.45 m and the shallowest 0.25 m; the largest among them is 15 m in diameter and the smallest one 2.5 m. Surface roughness shows that even though the seed point detection has captured sinkholes returns (Fig. 8a), not all detected points relate to them. The seed points were clustered into segments whose evolution is shown in Fig. 8b. Figure 8b also shows that, while the actual seed candidates converged into their respective boundary, the other candidates, which had no sinkhole characteristics, either shrunk into a polyline or were eliminated through the validation tests.

Applying the detection model for the complete dataset, ~350 sinkholes were identified (approximated due to sinkholes collapsing into one another, which can be counted as a single mega-sinkhole or a set of individual ones), with depth ranging from 0.25 to 18.45 m, and width from 1 to 35 m. Validation of these results was carried out by fieldwork in all the described sites and by aerial image analysis, particularly for mature sinkholes. Out of this amount, the proposed model missed only three. Additionally, six false sinkholes were detected. In terms of recall and precision rates

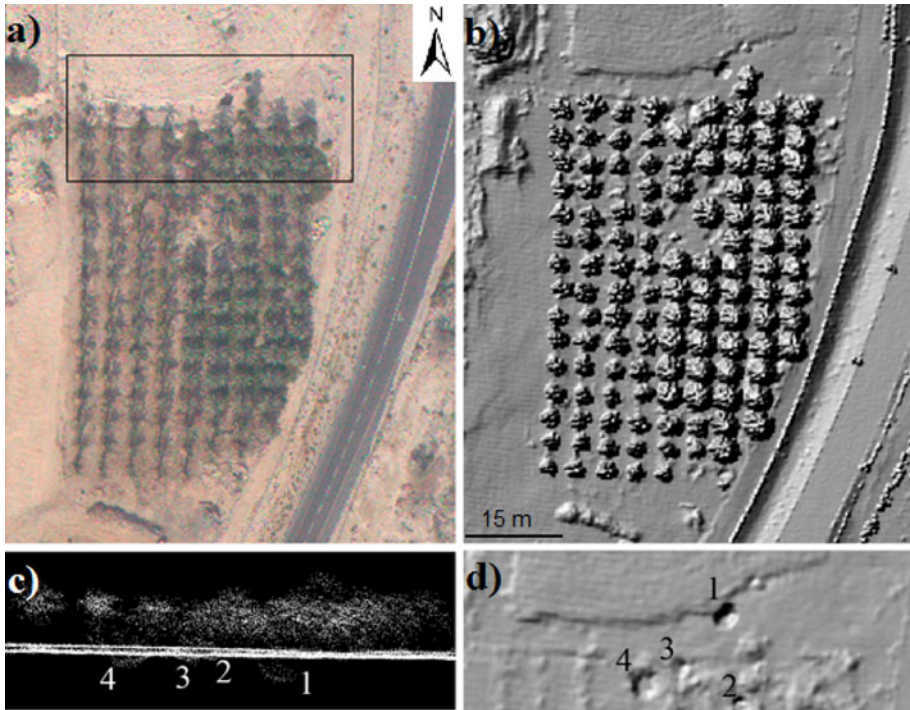


**Fig. 5** Sinkholes underneath tree canopies in the Ein-Gedi oasis (see Fig. 3b): **a** an aerial image of a palm plantation, showing no clear expression of any sinkhole; **b** a shaded relief map of the same region derived from the raw airborne laser scanning data, showing a clear expression of one sinkhole outside the plantation; **c** a side-looking view at the point-cloud revealing three more sinkhole inside the plantation; **d** a shaded relief formed after filtering the data showing the three other sinkholes

$$\text{Recall} = \frac{\text{TP}}{\text{TP} + \text{FN}} \quad (4)$$

$$\text{Precision} = \frac{\text{TP}}{\text{TP} + \text{FP}}$$

with TP—true positives, FP—false positive, FN—false negative, the proposed model reaches 98.76% and 97.54% levels, respectively. Both rates are high, considering the diverse sinkholes shapes and form and the surface roughness and clutter that characterizes the region. An increase of the depth threshold decreased the amount of false negatives, however, on the very clear expense of the number of false positives (Fig. 9). Decreasing the minimal detection level even further down showed on the other hand an increase in the false detections (Fig. 9).

#### 4.3 Comparison to photogrammetric mapping

To examine the quality of the laser-scanning based results, a comparison to manually detected sinkholes results using small-scale aerial photograph was carried out. Radiometric-related effects are the main cause either for false detection or for their under- or overestimation. False detections are usually ascribed to shrubs or small mounds that due to

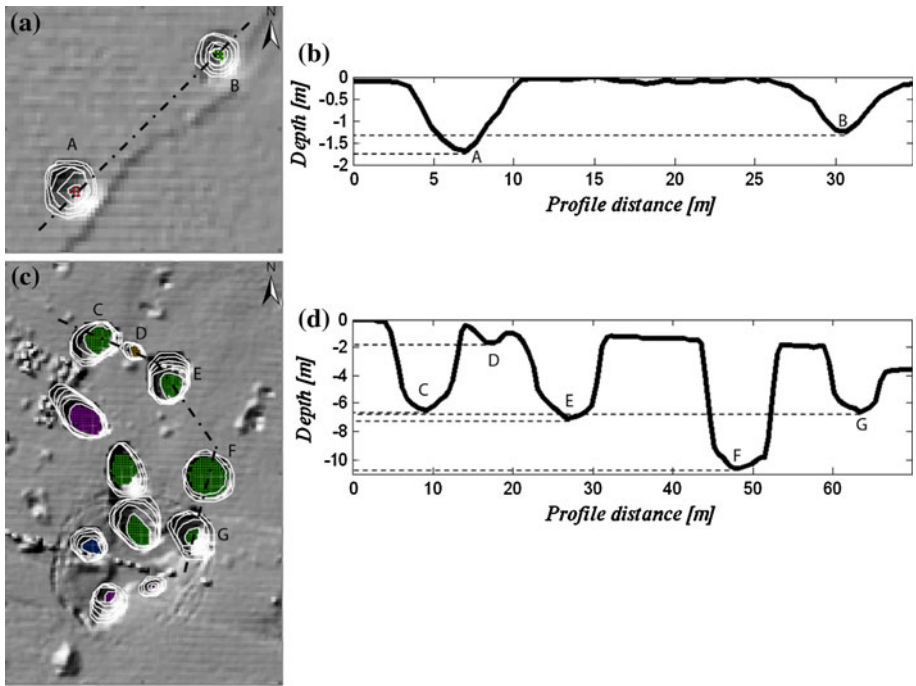


**Fig. 6** Illustration of the detection process in different sites, showing the seed points colored by their relevant scale, the active contour evolution, and a profile offering a side view of the sinkhole shapes: **a, b** Mineral Beach; **c, d** parking lot near the Ein-Gedi beach resort

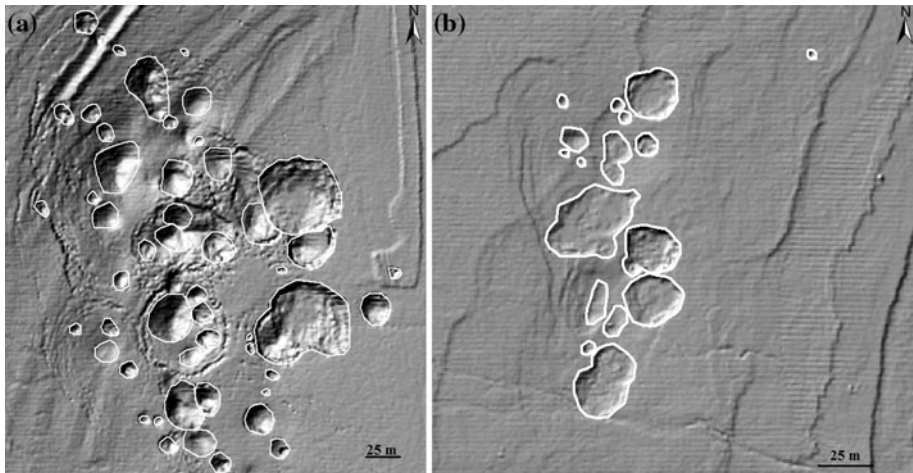


**Fig. 7** Application of the detection on sinkholes in Mineral Beach: **a** detection of a complex sinkhole field near the beach resort; **b** detection of sinkholes within mudflats, where sinkholes are shallow and can be of modest size

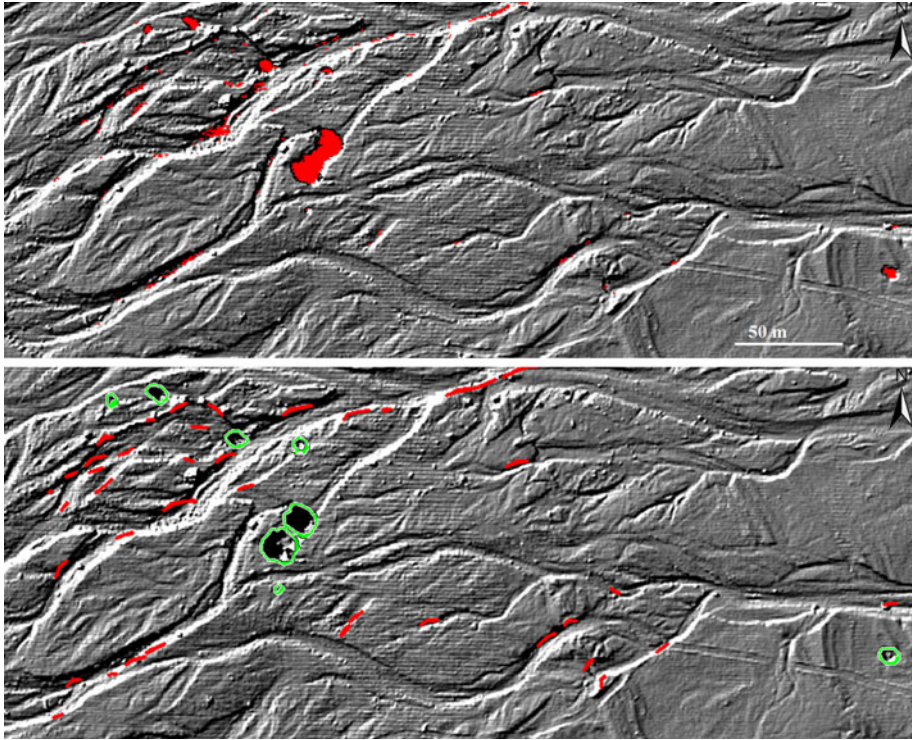


**Fig. 8** Detection of sinkholes within roughly textured terrain dissected by braided streams (Hever fan): **a** the detected seed points; **b** detected sinkholes following the boundary detection (*red* not sinkholes, *green* detected as sinkholes)

different light directions can be interpreted as depression areas instead of elevated ones (Fig. 10). Additionally, Fig. 10a shows that in small-scale aerial photographs, the exact sinkhole boundaries are not localized precisely, leading to only rough demarcation, and making evolution monitoring on the sinkhole-level infeasible, while overestimating its actual size. Another image-related shortcoming relates to cast shadows inside the sinkhole that leads to underestimation of the actual sinkhole depth. Comparative analysis of the lowest photogrammetrically derived sinkhole depth can be seen in Fig. 10c. Marked points were extracted from stereo models and are overlaid on top of the laser-scanning based reconstructed surface. All inner points (if any) fall on the sinkhole walls and do not reach their deepest part or bottom.

#### 4.4 Morphometric analysis

Other than the high detection rate, laser scanning data allow also extracting morphometric information about sinkholes both on the individual level and as a whole. Such information on such scale is essentially impossible to extract by any other means. We analyze the detected sinkholes through three aspects, the first relates to individual sinkhole properties, the second is of general metric attributes, and the third examines the interaction between sinkholes and other geomorphic features.

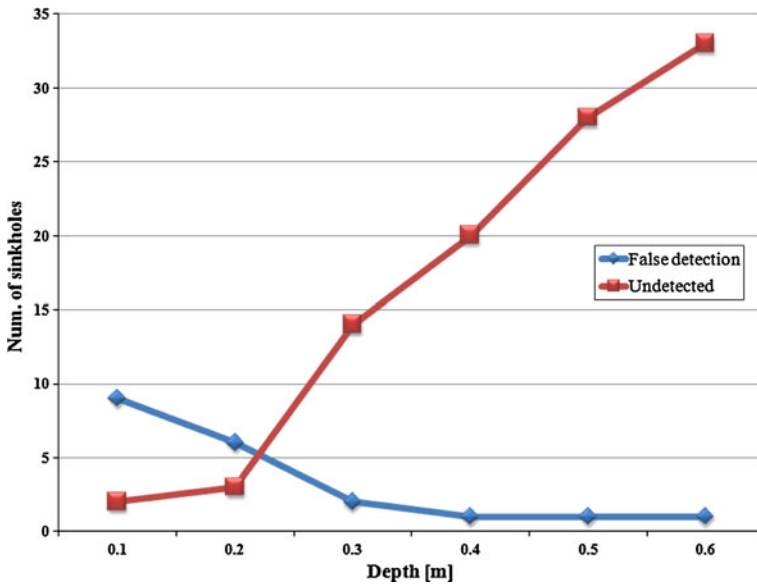


**Fig. 9** False-positive and true-negative levels as a function of the depth threshold

Information about individual sinkholes is provided in two “tiers” where the first provides metric information, including depth, area:

$$A = \frac{1}{2} \left| \sum_{i=1}^n x_i \cdot (y_{i+1} - y_{i-1}) \right| \tag{5}$$

with  $n$ , the number of boundary points, and  $x_i, y_i$  is their coordinates; perimeter and diameter. Additionally, the cavity volume,  $V$ , is estimated via:

$$V = \sum_{i=1}^n (h_{\max} - h_i) \cdot dx \cdot dy. \tag{6}$$

Volumetric information allows quantifying soil loss but also enables design of engineering solutions in sinkhole prone areas. The second tier measures offer characterization of the internal shape features. Shape-wise sinkholes are classified into cylindrical and bowl-like (see Fig. 11a–d). Predominantly, cylindrical sinkholes will be characterized by a sudden drop in height near their boundary, whereas a relatively continuous variation will characterize the bowl-like ones. Accordingly, the gradient strength within a sleeve surrounding sinkhole perimeter is analyzed. High values define cylindrical, whereas low values define bowl-like sinkholes (Fig. 12). For the cylindrical sinkholes, we also analyze the opening angle

$$\alpha = \tan^{-1} \left( \frac{\sqrt{A/\pi}}{d} \right) \tag{7}$$

as a means to assess the reliability of the laser scanner penetration capability with respect to the scanner opening angle. Generally, the reliability of the depth estimation relates to the potential viewing angle with narrower values for  $\alpha$  meaning a greater potential that the

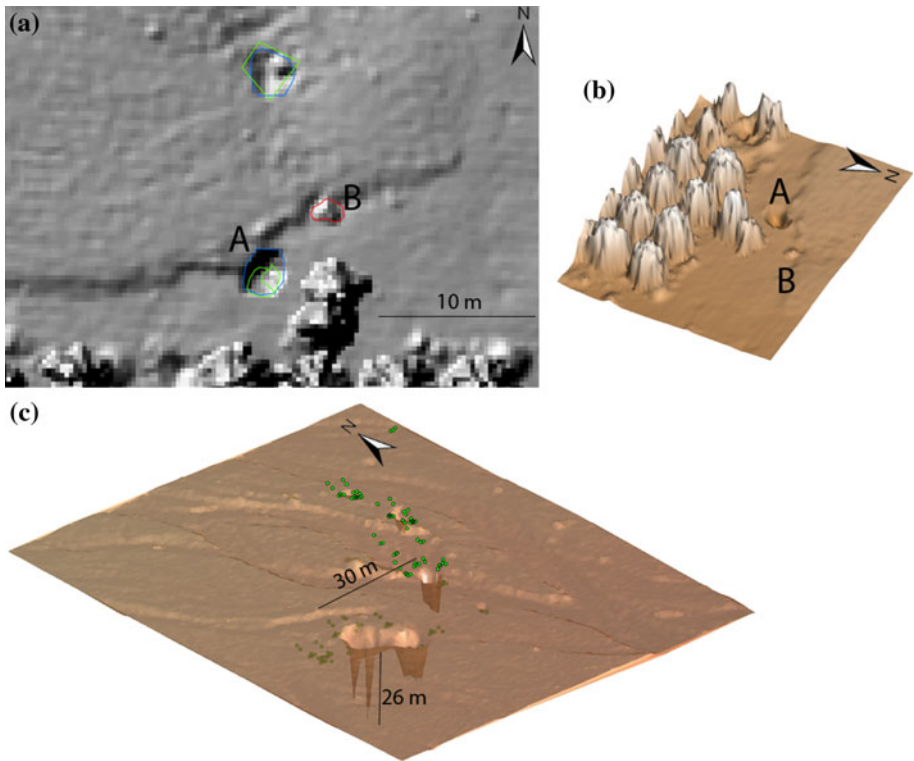


**Fig. 10** Comparative results of image and laser-scanning based extraction **a** results of image-based extraction (green + red) compared to data provided by the point cloud (blue); false detections can also be noticed (red); **b** 3D shaded-relief map of the site; **c** comparison of the extracted image-based 3D points and the laser scanning data, demonstrating limitation in depicting the inner sinkhole depth and geometry

range will relate to walls or to multi-paths. Our analysis shows that eight candidates have  $\alpha$  values smaller than  $25^\circ$ ; all of them are deeper than 5 m, leading us to place a caveat on their measured depth. The acquisition of three-dimensional data of the sinkholes inner part allows also characterizing the shape of their floor. This can be achieved by fitting a parametric representation to the floor-related returns. We test planar and bi-quadratic surfaces as descriptive models and decide between the two via standard model selection procedures (applying an  $F$  test). The floor-characterization reveals sinkholes in the Hever fan with a predominant directional inclination (Fig. 11e, f); all are clustered in one region.

Individual sinkhole attributes provide an insight into their overall characterization. In Fig. 13, the distribution of the sinkholes in relation to the surface elevation is shown. The clearest separation is between the alluvial sinkholes, those above the 400 m.b.m.s.l, and those below this level, which marks the initiation of a dramatic lake-level drop in the early 1980s. The ratio, in the surveyed areas, between sinkholes above and below 400 m.b.m.s.l is 70:170, respectively, showing that most sinkholes have been forming in the newly exposed plains. We also define another band ranging between 400 and 407 m.b.m.s.l, which can generally be regarded as a transition zone between the alluvial areas and the fine-grained mudflats. Figure 13 shows that the Ze'elim sinkholes are below

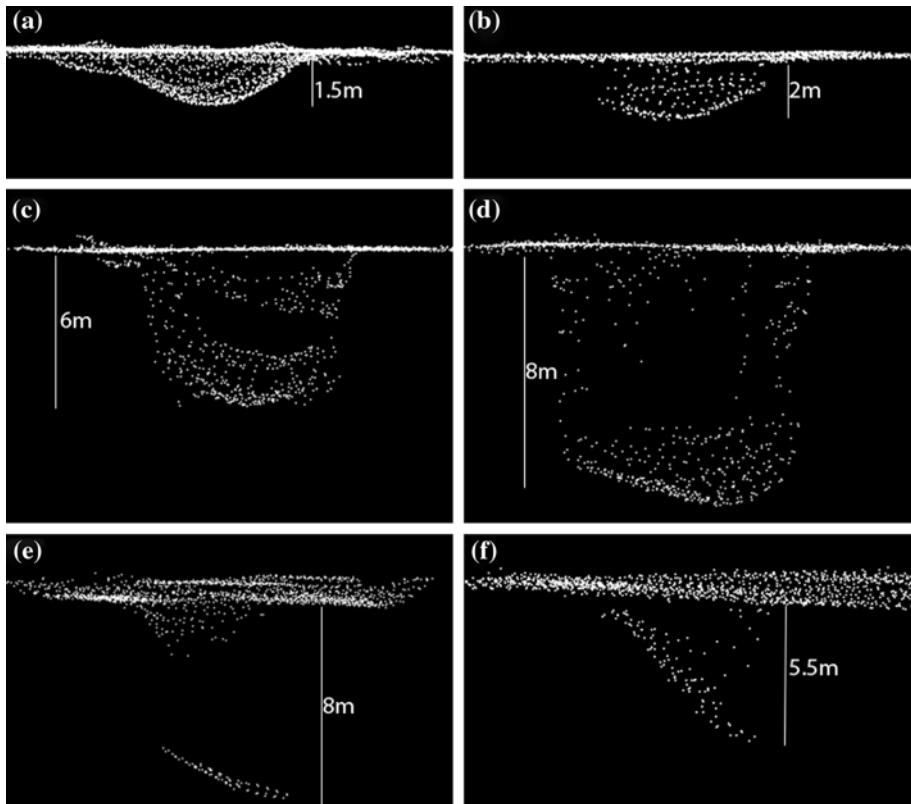
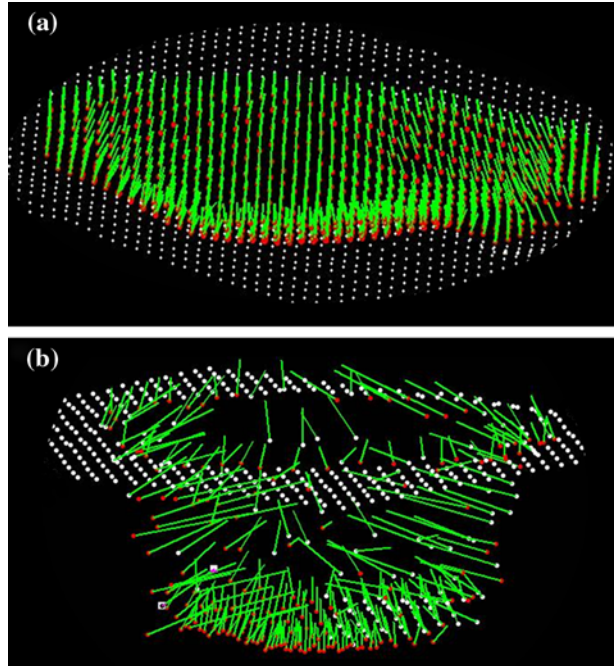


**Fig. 11** Detailed sinkhole shape characterization based upon the point cloud: **a, b** bowl shapes; **c, d** cylindrical shaped sinkholes; **e, f** sinkholes with slanted floor

the Dead Sea high stand level and are in the transition zone and the mudflats. In Hever, they appear above in the fan and the transition zone, and in Ein-Gedi, they are separated into “alluvial” and “mudflats” sinkholes. The comparison of mudflat sinkholes to the alluvial ones shows a clear difference between them by their average depth, where the “mudflats” are shallower than the “alluvials” (Fig. 14). Notice also that the depth dispersion is much more compact in the mudflat, with standard deviation of  $\pm 1$  m, compared to the alluvial ones where the dispersion reaches  $\pm 3.3$  m and has a thicker tail. There is also some correlation between the sinkholes depth and diameter, with shallower sinkholes having smaller diameter. This can be seen in Fig. 15. Figure 15 also shows that as sinkholes evolve, their diameter disperses; for sinkholes evolving within the mudflat, this spread is more controlled (a linear regression has yielded an R value of 0.6), but for the alluvial ones, the spread is much broader. An attempt to find correlation between the surface elevation and morphometric characteristics shows no clear relation that does not show up when separating the sinkholes into alluvials and mudflats. Particularly in the alluvial zones where sinkholes are deeper, the depth distribution shows no clear pattern. Similar study that correlated sinkhole parameters to their geographic location has shown no clear pattern. This correlation test was performed due to the understanding that sinkholes began evolving in the southern part of the Dead Sea and progressed northwards;

**Fig. 12** Normal distribution of inner sinkhole laser points, aimed at characterizing sinkhole shapes: **a** bowl-like; **b** cylindrical



therefore, the southern ones might be deeper (as being more mature) than the northern. These two tests indicate that while the underlying cause for sinkhole formation is common (dissolution of salt layers), their impact is relatively localized and not geographically related. Nonetheless, we point that in some of the regions under study (notably in Mineral, Hever, and Ze'elim), sinkholes have been forming along runoff channels (Fig. 16). This offers one of the best examples for interrelations between different geomorphic elements and the spatial relations between embryonic sinkholes, small and shallow gullies, as documented in the data. These high-resolution data therefore pave the way to a detailed study on the contribution of the surface runoff, generated in the Dead Sea coastal plain, transported by gullies toward the lake, and partly trapped behind the beach ridges, to the subsurface sinkholes generation.

## 5 Conclusions

We demonstrated an autonomous model for analyzing airborne laser scanning data, which facilitates the identification of incipient sinkholes and characterization of their evolution. Validation of the performance of the proposed model through ground survey and aerial photograph analysis show 98% level of accuracy. The model performs well under varying landforms and surface texture with little influence on the amount of extracted sinkholes. The research has managed showing detection ability of sinkholes in a variety of their evolution stages, starting a subtle  $\sim 1$ -m-wide depression and slowly developing as circular concentric fractures that evolve further into subsidence of the bottom and collapse of the surrounding walls. As the individual sinkholes evolve and grow, they often coalesce

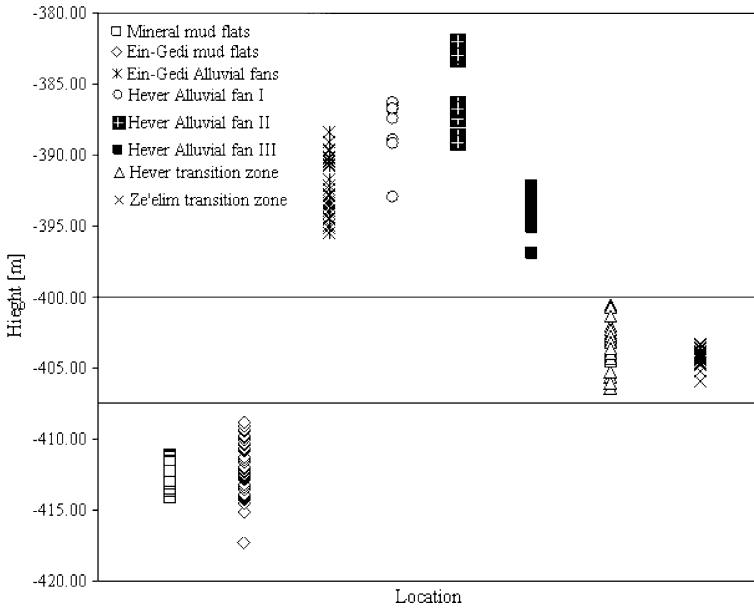
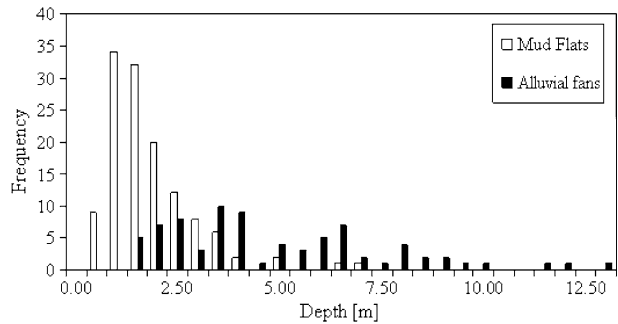


**Fig. 13** Distribution of sinkholes as a function of the surface elevation

**Fig. 14** Distribution of sinkhole depth with sinkhole categorized into mudflats and alluvial related



and form elongate depressions. The spatial distribution of sinkholes in the Dead Sea coastal plain shows that their formation accelerated when the water level dropped below 407 m.b.m.s.l., a level that commonly coincides with a transition between the coarse alluvial areas above and the fine-grained mudflats below. Over large regions, no other technology can provide such level of detail in three dimensions. Benefits of this type of information can be observed in detection ability, in the quantitative information that can be readily derived from the data, in the morphometric analysis, and the ability to identify interrelations among related phenomena. The detection ability of subtle features also means that more information than what is commonly extracted can be derived from laser point clouds autonomously, thereby extending and simplifying related analyses.

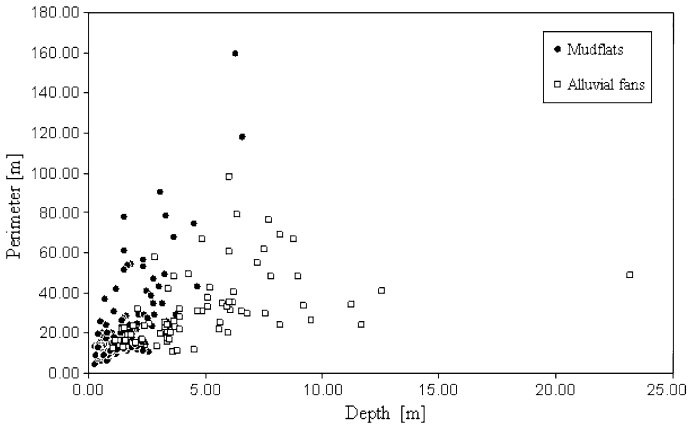


**Fig. 15** Distribution of the sinkhole depth as a function of their perimeter

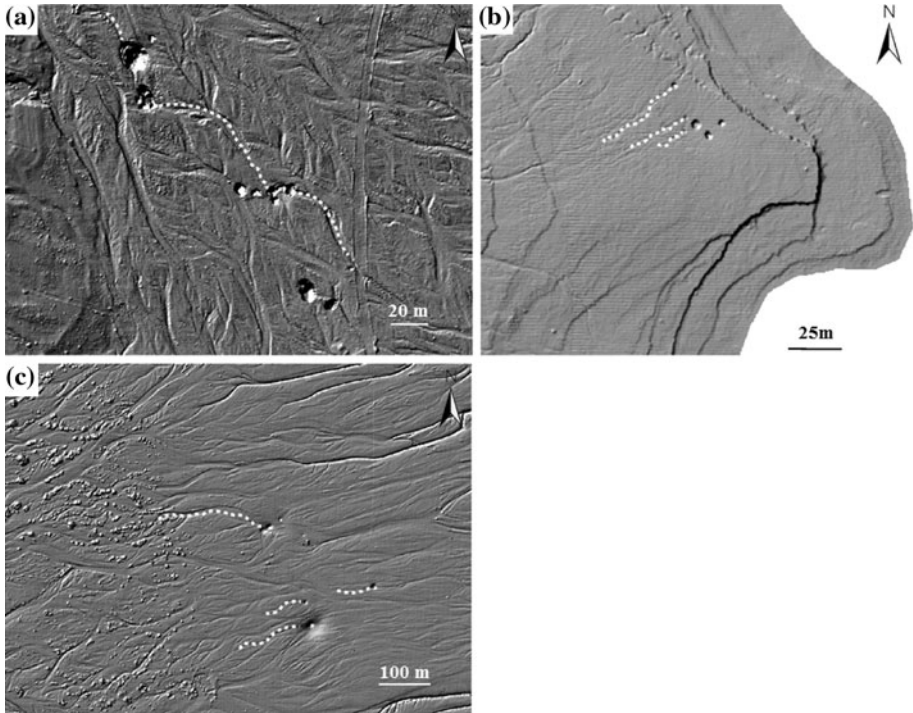


**Fig. 16** Examples for noticeable spatial relations between sinkholes and runoff water channels, shown in three different locations and sedimentary environments: **a** alluvial fan in Hever; **b** mudflats; **c** transition zone in the Ze'elim fan

**Acknowledgments** The research was funded in part by grants provided by the Israel Ministry of Science through the Dead Sea and Arava science center, the Israel Ministry of National Infrastructure, the Henri Gutwirth Fund for the Promotion of Research, the Geological Survey of Israel, and by the Israel Science Foundation grant #1539/08 to S. Marco.

## Appendix

Validation is carried out by further assessment and analysis of the sinkholes boundary and depth parameters. Those tests are aimed at quantifying sinkhole distinctiveness compared to its surrounding.

As the characterization phase is driven by external gradient related forces, the contour either adheres to the sinkhole boundary, or, if there is no clear transition between the minimum point and the surrounding, diverges or even crosses itself. Trapped area is measured by Eq. (5), and use of this quantity enables ensuring that contours do not collapse into a smaller area when fitted. Area is also linked with the contour perimeter via the compactness,  $C$ ,

$$C = \frac{l^2}{4\pi A} \tag{8}$$

which measures the similarity (and deviation) of the outer shape from circularity. Due to their concentric collapse pattern, most sinkholes form a generally circular shape with compactness value varying between 0.7 and 1 (circle compactness is one). To ensure depth distinctiveness, the relative sinkhole depth is evaluated by height differencing of the sinkhole deepest point from lowest perimeter point,

$$D = h_{\min}^{\text{perimeter}} - h_{\min}^{\text{sinkhole}} \tag{9}$$

Finally, sinkhole distinctiveness is measured by analyzing how a candidate sinkhole is embedded in its surrounding. This test is performed via a local bi-quadratic surface fitting

$$Z = ax^2 + by^2 + cxy + dx + ey + f \tag{10}$$

to the points surrounding the sinkhole and comparing the relative depth of each inner point to the adjusted surface. Regarding sinkholes as surface anomalies, the fitted surface is expected to “fail” predicting their actual depth. For “false” detections, which exhibit no anomalous surface behavior (otherwise they are holes), the deviations are expected to have a relatively small predication errors. To normalize the deviation error with respect to the varying sinkhole sizes, the mean difference,  $\bar{\delta}$ , is estimated by

$$\bar{\delta} = \frac{\sum_{i=1}^n (h_i^{\text{surface}} - h_i^{\text{measured}})}{n} \tag{11}$$

with  $h_i^{\text{surface}}$  the surface height,  $h_i^{\text{measured}}$  the original height, and  $n$  the number of points. For actual sinkholes, the adjusted surface should be relatively flat and the majority of the points lying underneath. Contrasting them, sinkholes whose mean difference is close to zero are either ones that alter signs (and therefore cancel the relative difference), or having an indistinct relative depth to the surrounding surface.

## References

Abelson M, Baer G, Shtivelman V, Wachs D, Raz E, Crouvi O, Kurzon I, Yeichieli Y (2003) Collapse-sinkholes and radar interferometry reveal neotectonics concealed within the Dead Sea. *Geophy Res Lett* 30(10):1545 52-1-4

- Abelson M, Yechieli Y, Crouvi O, Baer G, Wachs D, Bein A, Shtivelman V (2006) Evolution of the Dead Sea sinkholes. *Geol Soc Am Spec Pap* 401:241–253
- Akel N, Filin S, Doytsher Y (2007) orthogonal polynomials supported by region growing segmentation for the extraction of terrain from LiDAR Data. *Photogramm Eng Remote Sensing* 73(11):1253–1266
- Arkin Y, Gilat A (2000) Dead Sea sinkholes—an ever-developing hazard. *Environ Geol* 39(7):711–722
- Baer G, Schattner U, Wachs D, Sandwell D, Wdowski S, Frydman S (2002) The lowest place on Earth is subsiding—an InSAR (interferometric synthetic aperture radar) perspective. *Geol Soc Am Bull* 114(1):12–23
- Besl PJ (1988) *Surfaces in range image understanding*. Springer-Verlag, New York
- Buttrick D, Schalkwyk AV (1998) Hazard and risk assessment for sinkhole formation on dolomite land in South Africa. *Environ Geol* 36(1–2):170–178
- Closson D (2005) Structural control of sinkholes and subsidence hazards along the Jordanian Dead Sea coast. *Environ Geol* 47:290–301
- Closson D, Abou Karaki N, Hansen H, Derauw D, Barbier C, Ozer A (2003) Space-borne radar interferometric mapping of precursory deformations of a dyke collapse—Dead Sea area—Jordan. *Int J Remote Sens* 24(4):843–849
- Hall JK (1994) Digital shaded-relief map of Israel and environs 1:500,000: Israel Geological Survey
- Kass M, Witkin A, Terzopoulos D (1988) Snakes: active contour models. *Int J Comput Vis* 1:321–331
- Kaufmann O, Quinif Y (2002) Geohazard map of cover-collapse sinkholes in the ‘Tournaisis’ area, southern Belgium. *Eng Geol* 65:117–124
- Martínez JD, Johnson KS, Neal JT (1998) Sinkholes in evaporite rocks. *Am Sci* 86:38–51
- Neal JT, Johnson KS (2002) McCauley sink: a compound breccia pipe in evaporite Karst, Holbrook basin, Arizona, USA. *Carbonates Evaporites* 17:98–106
- Nichol D (1998) Sinkholes at Glan Lllyn on the A55 North Wales Coast Road, UK. *Eng Geol* 50:101–109
- Salvati R, Sasowsky ID (2002) Development of collapse sinkholes in areas of groundwater discharge. *J Hydrol* 264(1–4):1–11
- Tharp TM (1999) Mechanics of upward propagation of cover-collapse sinkholes. *Eng Geol* 52(1–2):23–33
- Yechieli Y, Abelson M, Wachs D, Shtivelman V, Crouvi O, Baer G (2003) Formation of sinkholes along the shore of the Dead Sea—preliminary investigation. In: Beck BF (ed) 9th Multidisciplinary conference on sinkholes and the engineering and environmental impacts of Karst, Huntsville, Alabama, USA: 184–194
- Yechieli Y, Abelson M, Bein A, Crouvi O, Shtivelman V (2006) Sinkhole “swarms” along the Dead Sea coast: reflection of disturbance of lake and adjacent groundwater systems. *Geol Soc Am Bull* 118(9/10):1075–1087